Room-Temperature Anisotropic Plasma Mirror and Polarization-Controlled Optical Switch Based on Type-II Weyl Semimetal WP$_2$

Kaixuan Zhang,[1] Yongping Du,[2] Zeming Qi,[3] Bin Cheng,[1] Xiaodong Fan [,1] Laiming Wei,[1,*] Lin Li,[1]
Dongli Wang,[1] Guolin Yu,[4] Shuhong Hu,[4] Changhong Sun,[4] Zhiming Huang,[4] Junhao Chu,[4]
Xiangang Wan,[5] and Changgan Zeng[1,†]

[1]*International Center for Quantum Design of Functional Materials, Hefei National Laboratory for Physical Sciences at the Microscale, CAS Key Laboratory of Strongly Coupled Quantum Matter Physics, Department of Physics, and Synergetic Innovation Center of Quantum Information and Quantum Physics, University of Science and Technology of China, Hefei, Anhui 230026, China*

[2]*Department of Applied Physics and Institution of Energy and Microstructure, Nanjing University of Science and Technology, Nanjing, Jiangsu 210094, China*

[3]*National Synchrotron Radiation Laboratory, University of Science and Technology of China, Hefei, Anhui 230029, China*

[4]*National Laboratory for Infrared Physics, Shanghai Institute of Technical Physics, Chinese Academy of Sciences, Shanghai 200083, China*

[5]*National Laboratory of Solid State Microstructures, Department of Physics, and Collaborative Innovation Center of Advanced Microstructures, Nanjing University, Nanjing, Jiangsu 210093, China*

Anisotropy in electronic structures may ignite intriguing anisotropic optical responses, as has been well demonstrated in various systems including superconductors, semiconductors, and even topological Weyl semimetals. Meanwhile, it is well established in metal optics that the metal reflectance declines from one to zero when the photon frequency is above the plasma frequency ω_p, behaving as a plasma mirror. However, the exploration of anisotropic plasma mirrors and corresponding applications remains elusive, especially at room temperature. Here, we discover a pronounced anisotropic plasma reflectance edge in the type-II Weyl semimetal WP$_2$, with an anisotropy ratio of ω_p up to 1.5. Such anisotropic plasma mirror behavior and its robustness against temperature promise optical device applications over a wide temperature range. For example, the high sensitivity of polarization-resolved plasma reflectance edge renders WP$_2$ an inherent polarization detector. We further achieve a room-temperature WP$_2$-based optical switch, effectively controlled by simply tuning the light polarization. These findings extend the frontiers of metal optics as a discipline and promise the design of multifunctional devices combining both topological and optical features.

I. INTRODUCTION

Anisotropies in atomic and electronic structures have been discovered to spark an array of intriguing physical phenomena, including anisotropic optical responses [1–12]. For example, anisotropic optical conductivity was revealed in the parent compounds of iron arsenide superconductors, arising from the anisotropic energy gap opening [1]. Anisotropic optical absorption and photoluminescence were also discovered in two-dimensional black phosphorus semiconductor, and were attributed to the anisotropies in selection rule and effective mass [3–5]. Recently, anisotropic photocurrent responses were

unveiled in Weyl semimetals owing to the chirality selection rule and asymmetric Pauli blockade in finitely tilted Weyl cones [8,9].

On the other hand, metals can be regarded as plasma mirrors, with the reflectance edge determined by the plasma frequency $\omega_p = \sqrt{ne^2/\epsilon_0 m^*}$ [13,14], where n is the carrier density, e is the elementary charge, ϵ_0 is the vacuum permittivity, and m^* is the effective mass. Usually, metals possess nearly isotropic Fermi surfaces and the corresponding isotropic plasma reflectance edge [13,14]. In contrast, some semimetals possess highly anisotropic Fermi surfaces, such as bismuth [15,16] and WTe$_2$ [17–20], which are expected to exhibit anisotropic plasma edges. These semimetals, however, possess low ω_p, thus preventing the achievement of anisotropic plasma mirrors at high temperatures. Recently, WP$_2$ was theoretically predicted

*weilm203@mail.ustc.edu.cn
†cgzeng@ustc.edu.cn

to be a robust type-II Weyl semimetal [21] with highly anisotropic Fermi surfaces [21–23]. Herein, we describe the discovery of an anisotropic plasma reflectance edge in WP$_2$, which is pronounced even at room temperature, and further demonstrate a typical application of a polarization-controlled optical switch.

II. RESULTS AND DISCUSSION

A. Structure characterization of WP$_2$

WP$_2$ single crystals with orthorhombic structure [β-phase, Fig. 1(a)] are grown via chemical vapor transport [24] (see more details in the Supplemental Material (SM) [25]). Figure 1(b) depicts several natural crystal faces including the (010), (062), and (021) surfaces. The high quality of the WP$_2$ single crystals at atomic and macroscopic scales are demonstrated by transmission electron microscopy (TEM) [Fig. 1(c)], scanning tunneling microscopy (STM) [Fig. 1(d)], and x-ray diffraction (XRD) patterns [Figs. 1(e) and 1(f)].

B. Room-temperature anisotropic plasma mirror behavior of WP$_2$

Polarization-resolved reflectance spectra are measured by Fourier-transform infrared spectrometry. The light polarization E is rotated in the (001) plane to measure the reflectance spectra for E parallel to the crystallographic a and b axes, and is rotated in the (010) plane to measure the spectra for E along the a and c axes. Figures 2(a) and 2(b) show a well-defined sharp reflectance edge emerging in these spectra, followed by a reflectance valley denoted

as V_a at $\sim$3600 cm^{-1} for $E||a$, V_b at $\sim$2700 cm^{-1} for $E||b$, and V_c at $\sim$4000 cm^{-1} for $E||c$. A reflectance valley typically develops near the screened plasma frequency $\omega_p^* = \omega_p/\sqrt{\epsilon_\infty}$, where ϵ_∞ is the permittivity at high frequency [16]. Therefore, the varied valley wave numbers for $E||a$, $E||b$, and $E||c$ reflect anisotropy in the plasma frequency.

Quantitative analysis of the plasma frequency is accomplished by using the RefFIT program [26] to fit the reflectance curves according to the two-Drude model [19] with the complex dielectric function:

$$\epsilon(\omega) = \epsilon_\infty - \sum_{j=1}^{2} \frac{\omega_{p,j}^2}{\omega^2 + i\omega/\tau_j} + \sum_k \frac{\Omega_{p,k}^2}{\omega_{0,k}^2 - \omega^2 - i\omega\gamma_k},$$

where $\omega_{p,j}$ are the free carrier plasma frequencies for electrons and holes, τ_j are the free carrier scattering times for electrons and holes, $\Omega_{p,k}$ are the oscillator strengths for phonons and interband electronic transitions, $\omega_{0,k}$ are the phonon and interband transition frequencies, and γ_k is the width of the corresponding transition (see more details in Table S1). The bare plasma frequencies [20] for $E||a$, $E||b$, and $E||c$ are $\omega_{p,a}^2 = \omega_{p,a,1}^2 + \omega_{p,a,2}^2$, $\omega_{p,b}^2 = \omega_{p,b,1}^2 + \omega_{p,b,2}^2$, and $\omega_{p,c}^2 = \omega_{p,c,1}^2 + \omega_{p,c,2}^2$, respectively. The fitting curves for $E||a$, $E||b$, and $E||c$ are plotted with thick gray curves in Figs. 2(a) and 2(b). The ω_p values estimated from the two-Drude fitting model are displayed in Fig. 2(c) (circles), which illustrate strong anisotropies for $E||a$, $E||b$, and $E||c$. For example, $\omega_{p,a}/\omega_{p,b}$ and $\omega_{p,c}/\omega_{p,b}$ are about 1.35 and 1.46, consistent with the valley wave number ratios $V_a:V_b$ ($\sim$1.33) and $V_c:V_b$ ($\sim$1.48), respectively.
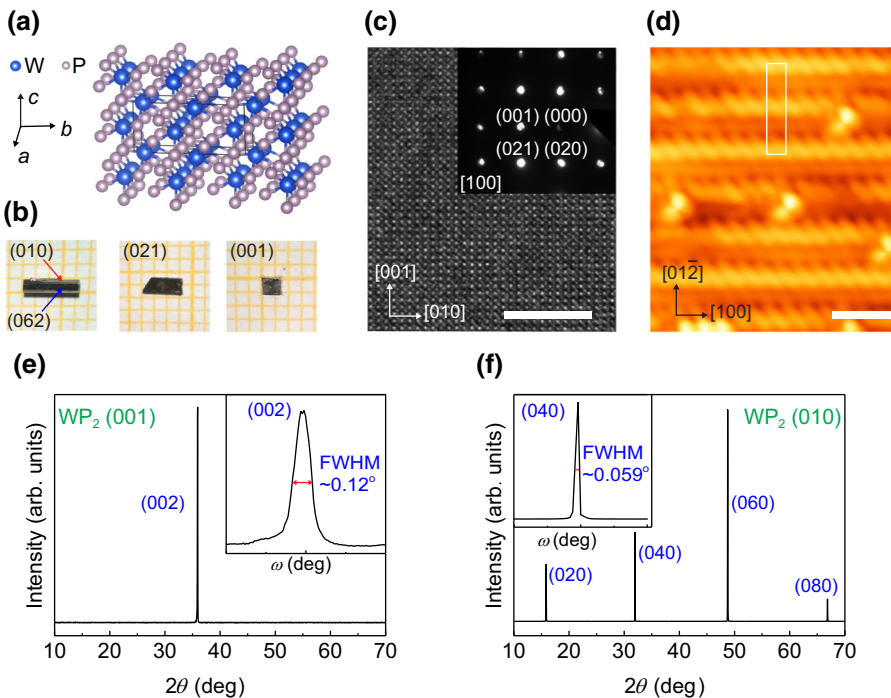

FIG. 1. Structure characterizations of WP$_2$. (a) Crystallographic structure. The black lines indicate a unit cell. (b) Optical images of the samples with different crystalline surfaces adopted for XRD and optical reflectance measurements. The orange squares in the background are 1×1 mm^2. (c) TEM and selected area electron diffraction images along the [100] direction. The scale bar is 6 nm. (d) Atomic-resolution STM image of the cleaved (021) surface. The white rectangle denotes a surface unit cell. The scale bar is 1 nm. (e),(f) XRD patterns on the (001) and (010) surfaces, respectively. The insets show the rocking curves with a small full width at half maximum (FWHM).
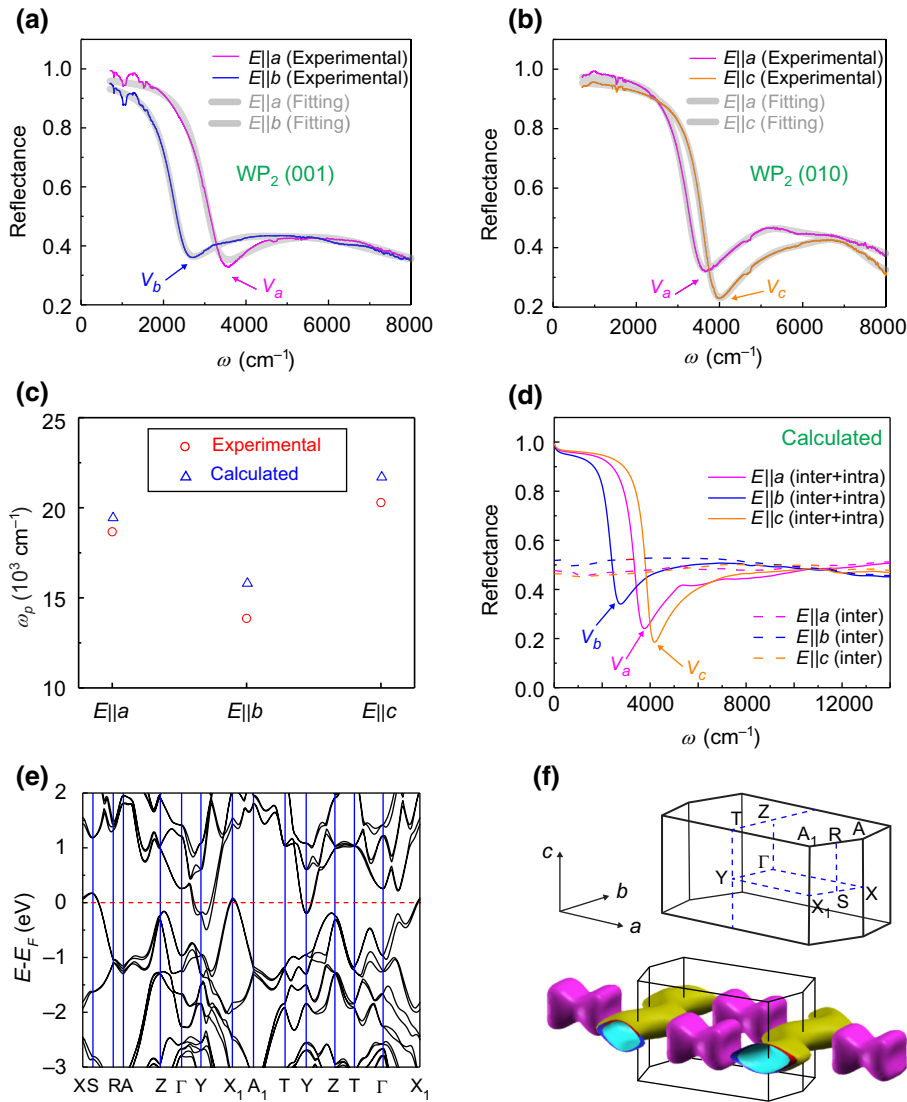
FIG. 2. Anisotropic reflectance and electronic structures of WP_2. (a),(b) Measured reflectance spectra of the (001) and (010) surfaces, respectively. The light polarization E in (a) is parallel to the a (pink) and b axes (blue), whereas E in (b) is parallel to the a (pink) and c axes (yellow). The pink, blue, and yellow arrows indicate the reflectance valleys for $E||a$ (V_a), $E||b$ (V_b), and $E||c$ (V_c), respectively. The gray curves are the fitting curves based on the two-Drude model. (c) Plot of ω_p extracted from fitting the experimental data (circles) and from theoretical calculations (triangles), respectively. (d) Calculated reflectance spectra for $E||a$ (pink), $E||b$ (blue), and $E||c$ (yellow), respectively. The solid curves take into account both the intraband and interband excitations, whereas the dashed curves consider only interband excitations. (e) Calculated band structures along high-symmetry directions. (f) Calculated Fermi surfaces. The bow-tie-shaped closed pockets are electron Fermi surfaces, whereas the spaghetti-shaped open pockets are hole Fermi surfaces.

The sharp reflectance edge revealed here suggests that the interband excitations are well separated from the plasma edge. By contrast, some metals such as copper exhibit smeared reflectance edges that is considerably mixed with the pronounced interband electronic transition [13]. To reinforce this point, theoretical calculations are performed (see more details in the SM [25]). When only interband excitations are considered, a clear reflectance edge is absent in the calculated reflectance spectra [see the dashed curves in Fig. 2(d)]. When the intraband excitations are taken into account, the calculated spectra exhibit sharp and anisotropic reflectance edges, with the reflectance valley wave numbers approximating those of experimental measurements [see solid curves in Fig. 2(d)].

Figure 2(c) shows that the ω_p values extracted by fitting the experimental data (circles) are consistent with theoretical predictions (triangles). The effective mass, which is extracted from the formula $\omega_p^2 = ne^2/\epsilon_0 m^*$, reaches its maximum along the b axis with a mass anisotropy

ratio $\eta_{ab} = m_b^*/m_a^* = \omega_{p,a}^2/\omega_{p,b}^2 \sim 1.8$, which is qualitatively comparable with the calculated value of $\eta_{ab} \sim 1.5$ [Fig. 2(c)]. This mass anisotropy can be attributed to the underlying anisotropy of the band structures and Fermi surfaces. Figure 2(e) shows that the hole pocket dispersion is much flatter along the X-S (b axis) direction than the S-R (c axis) and Y-X_1 (a axis) directions, and the electron pocket dispersion is slightly flatter along the G-Y (b axis) direction than the Y-T (c axis) and Y-X_1 (a axis) directions. Moreover, the hole Fermi surfaces are open and possess a spaghettilike structure that extends along the b direction [Fig. 2(f)]. Therefore, the band mass is naturally expected to be largest along the b axis, which corresponds to a plasma frequency that is smallest along the b axis, in agreement with the experimental observations [Fig. 2(c)]. However, we cannot distinguish between the contributions of the electrons and holes at the present stage. It is well known that type-II Weyl semimetals are characterized by a significantly tilted Weyl cone with highly anisotropic band

dispersions [27,28]. Both the anisotropic plasma edge and anisotropic Weyl cone are manifestations of the anisotropic electronic structure, which are essentially rooted in the anisotropic atomic structure of WP$_2$.

According to Fig. 3(a), as the angle (θ) between E and the a axis increases from 0° to 90°, the plasma reflectance edge of the (001) surface evolves from a single valley (V_a) into double valleys (V_a and V_b), and then finally into a single valley (V_b) [see more data for the (001), (010), (021), and (062) surfaces in Figs. S1, S3, and S4, and additional discussion in the SM [25]]. At an intermediate polarization angle, the electric field can be decomposed into two orthogonal directions along the a and b axes. Therefore, the reflectance can be estimated by the formula $R(\theta) = R(E||a)\cos^2\theta + R(E||b)\sin^2\theta$, where $R(E||a)$ and $R(E||b)$ are the measured reflectance values at $\theta = 0°$ and $\theta = 90°$, respectively. The estimated reflectances obtained from this formula are nearly identical to experimentally measured values, as shown in Fig. S2 of the SM [25].

Reflectance anisotropy is more clearly manifested in the θ-dependent reflectances at energies near the reflectance edge. Figures 3(b) and 3(c) show the reflectance as a function of θ when the wave numbers are fixed at those of the reflectance valleys V_a (~ 3600 cm^{-1}) and V_b (~ 2700 cm^{-1}). The experimental results reveal a twofold symmetry, which are consistent with the estimated results obtained from $R(\theta) = R(E||a)\cos^2\theta + R(E||b)\sin^2\theta$. Such polarization-sensitive anisotropic

reflectance renders the WP$_2$ an inherent polarization analyzer to detect the light polarization direction. More importantly, by simply tuning the incident light polarization, the reflected light quantity by WP$_2$ is controlled effectively. For example, the reflectance of WP$_2$ at ~ 2700 cm^{-1} declines from approximately 75% to around 35% as the polarization angle θ rotates from 0° ($E||a$) to 90° ($E||b$) [see the blue curve in Fig. 3(b)]. Such a large modulation of the reflectance (or reflected light quantity) renders WP$_2$ itself an interesting concept of prototypical polarization-controlled optical switch based on the mechanism of the polarization-dependent anisotropic plasma edge (see further discussion in notes 3 and 4 of the SM [25]).

Next, we investigate the temperature dependence of the plasma edge, using the WP$_2$ (021) surface with $E||a$ as an example. As shown in Fig. 4(a), the plasma edges are nearly identical across a range of temperatures spanning 300 K down to 5 K. The electron and hole pockets and the corresponding carrier density of WP$_2$ are relatively large, thereby tuning the plasma edge into an energy range of 0.2–0.5 eV. This energy range of the plasma edge is much higher than that of typical semimetals investigated previously (e.g., <0.08 eV for bismuth [15,16] and WTe$_2$ [19,20]). Furthermore, the sharp plasma reflectance edges of WP$_2$ are located away from the interband transitions [Fig. 2(d)]. Both factors may render the plasma edge insensitive to temperature, which facilitates the manipulation and utilization of the reflected light spectrum of
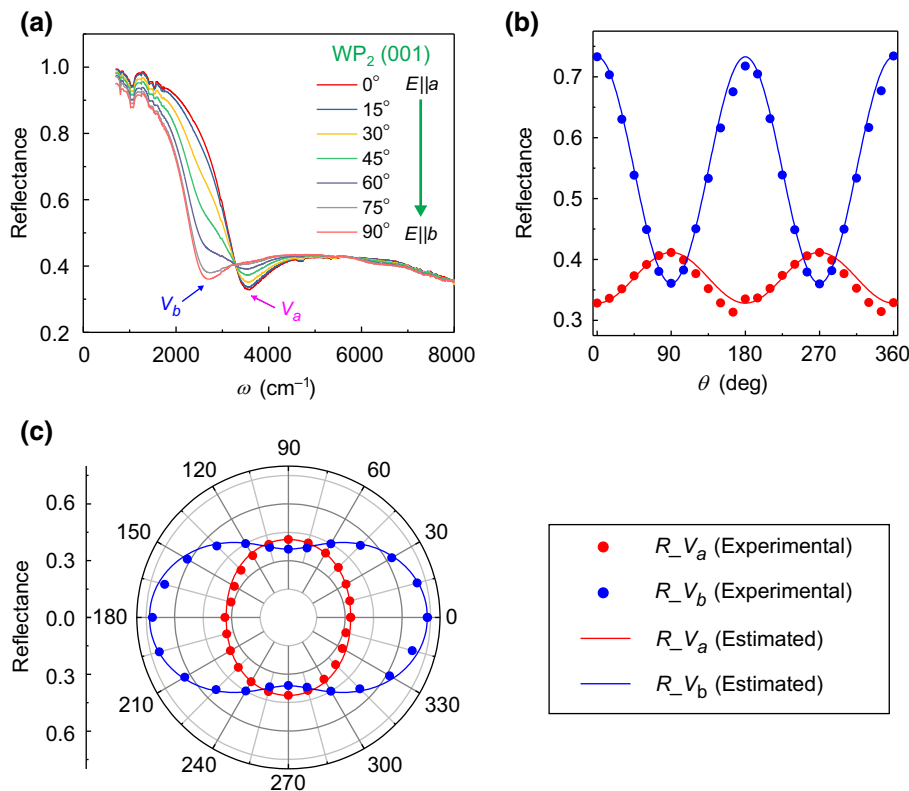

(a)

(b)

(c)

FIG. 3. Polarization-resolved anisotropic reflectance of the WP$_2$ (001) surface. (a) Reflectance spectra at various polarization angles θ, where θ denotes the angle between the light polarization direction (direction of electrical field E) and the a axis. Reflectance valleys V_a and V_b are indicated by the arrows. (b) Measured reflectances at the wave numbers of reflectance valleys V_a (~ 3600 cm^{-1}, red circles) and V_b (~ 2700 cm^{-1}, blue circles). The corresponding estimated reflectances are depicted as red and blue solid curves, respectively. (c) Polar plot of the measured and estimated reflectances from (b).
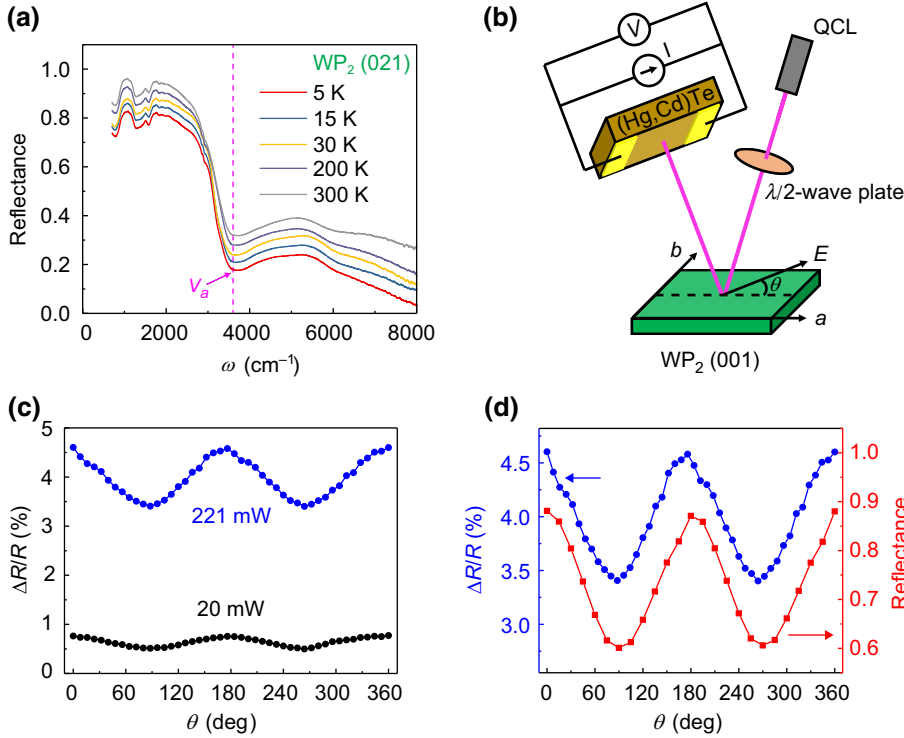
FIG. 4. Polarization-controlled optical switch based on WP_2. (a) Reflectance spectra of the (021) surface at various temperatures. The curves are shifted vertically for clarity. The light polarization is along the a axis. (b) Schematic of the polarization-controlled optical switch apparatus. (c) Relative resistance change $\Delta R/R$ of the (Hg,Cd)Te thin film as a function of θ, as induced by the reflected light of the WP_2 (001) surface. The laser wavelength and wave number are 4.57 μm and 2188 cm^{-1}, and the output power of the quantum cascade laser (QCL) is 20 mW (black circles) and 221 mW (blue circles), respectively. (d) Plot of $\Delta R/R$ (blue circles) as a function of θ, where laser power is 221 mW and measurements are taken at room temperature. The measured reflectance (red squares) of the WP_2 (001) surface at 2188 cm^{-1} as a function of θ at room temperature.

WP_2 over a wide temperature range. As a result, WP_2 is a promising material for application toward multifunctional (e.g., polarization detection and control) photonic and optoelectronic devices. It is noted that other topological semimetals, such as nodal-line semimetals, can also possess intrinsically large anisotropy and large Fermi surfaces at the same time [29,30], which may also promise anisotropic plasma mirror behavior and corresponding applications, and thus extend our findings toward even broader prospects.

C. Polarization-controlled optical switch application of WP_2

Now, we demonstrate the polarization-controlled optical switch function of WP_2 by using the photoconductive effect of the (Hg,Cd)Te semiconductor. As depicted in Fig. 4(b), a linearly polarized laser is rotated by a $\lambda/2$-wave plate and subsequently reflected by the WP_2 (001) surface before it finally arrives at a target (Hg,Cd)Te thin film (see further details in the SM [25]). The adopted laser wavelength is 4.57 μm, corresponding to a wave number of 2188 cm^{-1} (see more discussions in note 5 of the SM [25]). Here we define the relative change of the (Hg,Cd)Te resistance as $\Delta R/R = (R_1 - R_2)/R_1$, where R_1 and R_2 are the resistances before and after illumination, respectively. Figure 4(c) depicts $\Delta R/R$ as a function of θ with different laser powers. It is evident that $\Delta R/R$ oscillates with θ, reaches a maximum near 0° and 180°, and declines to a minimum near 90° and 270°. Interestingly, as shown in Fig. 4(d), the period and phase of such $\Delta R/R$

oscillations are in excellent agreement with those of the reflectance oscillations of the WP_2 (001) surface. Moreover, no periodic oscillations of $\Delta R/R$ are observed when WP_2 is replaced by a gold film. Therefore, the $\Delta R/R$ oscillations of the (Hg,Cd)Te can be unambiguously attributed to the polarization-dependent plasma reflectance edge of WP_2. The consistence between the resistance oscillations of (Hg,Cd)Te and reflectance oscillations of WP_2, in turn, validate the optical switch function of WP_2. We emphasize that WP_2 itself, instead of (Hg,Cd)Te, functions as an optical switch, and the present experiment is a prototypical example rather than the optimal case of the practical device applications.

The previously investigated optical switches usually consist of complex structures [31]. For example, some optomechanical switches are based on microelectromechanical systems, which require micro-nano manufacture [31]. By contrast, here we demonstrate an attractive and simple polarization-controlled optical switch, which is present in single crystals and can be exploited by taking full advantage of the anisotropic plasma edge of the Weyl semimetal WP_2.

III. CONCLUSION

In summary, we reveal a pronounced anisotropic plasma reflectance edge in the topological type-II Weyl semimetal WP_2, which arises from the corresponding anisotropic electronic structures and is robust against temperature. Moreover, utilizing such polarization-sensitive anisotropic plasma mirror behavior, we achieve a room-temperature

WP$_2$-based optical switch, which is effectively controlled by simply tuning the light polarization. The revelation of the anisotropic plasma reflectance edge and the polarization-controlled optical switch not only extend the frontiers of metal optics, but also open the door to intriguing optical applications based on anisotropic topological semimetals.

---

[1] M. Nakajima, T. Liang, S. Ishida, Y. Tomioka, K. Kihou, C. H. Lee, A. Iyo, H. Eisaki, T. Kakeshita, T. Ito, and S. Uchida, Unprecedented anisotropic metallic state in undoped iron arsenide BaFe$_2$As$_2$ revealed by optical spectroscopy, Proc. Natl. Acad. Sci. U.S.A. **108,** 12238 (2011).

[2] M. Guarise, B. Dalla Piazza, H. Berger, E. Giannini, T. Schmitt, H. M. Ronnow, G. A. Sawatzky, J. van den Brink, D. Altenfeld, I. Eremin, and M. Grioni, Anisotropic softening of magnetic excitations along the nodal direction in superconducting cuprates, Nat. Commun. **5,** 5760 (2014).

[3] J. Qiao, X. Kong, Z. X. Hu, F. Yang, and W. Ji, High-mobility transport anisotropy and linear dichroism in few-layer black phosphorus, Nat. Commun. **5,** 4475 (2014).

[4] X. Wang, A. M. Jones, K. L. Seyler, V. Tran, Y. Jia, H. Zhao, H. Wang, L. Yang, X. Xu, and F. Xia, Highly anisotropic and robust excitons in monolayer black phosphorus, Nat. Nanotechnol. **10,** 517 (2015).

[5] L. Li, J. Kim, C. Jin, G. J. Ye, D. Y. Qiu, F. H. da Jornada, Z. Shi, L. Chen, Z. Zhang, F. Yang, K. Watanabe, T. Taniguchi, W. Ren, S. G. Louie, X. H. Chen, Y. Zhang, and F. Wang, Direct observation of the layer-dependent electronic structure in phosphorene, Nat. Nanotechnol. **12,** 21 (2016).

[6] Y. Chen *et al.*, Black arsenic: A layered semiconductor with extreme in-plane anisotropy, Adv. Mater. **30,** e1800754 (2018).

[7] L. Li, P. Gong, D. Sheng, S. Wang, W. Wang, X. Zhu, X. Shi, F. Wang, W. Han, S. Yang, K. Liu, H. Li, and T. Zhai, Highly in-plane anisotropic 2D GeAs$_2$ for polarization-sensitive photodetection, Adv. Mater. **30,** e1804541 (2018).

[8] Q. Ma, S.-Y. Xu, C.-K. Chan, C.-L. Zhang, G. Chang, Y. Lin, W. Xie, T. Palacios, H. Lin, S. Jia, P. A. Lee, P. Jarillo-Herrero, and N. Gedik, Direct optical detection of Weyl fermion chirality in a topological semimetal, Nat. Phys. **13,** 842 (2017).

[9] J. Ma, Q. Gu, Y. Liu, J. Lai, P. Yu, X. Zhuo, Z. Liu, J. H. Chen, J. Feng, and D. Sun, Nonlinear photoresponse of type-II Weyl semimetals, Nat. Mater. **18,** 476 (2019).

[10] G. B. Osterhoudt, L. K. Diebel, M. J. Gray, X. Yang, J. Stanco, X. Huang, B. Shen, N. Ni, P. J. W. Moll, Y. Ran, and K. S. Burch, Colossal mid-infrared bulk photovoltaic effect in a type-I Weyl semimetal, Nat. Mater. **18,** 471 (2019).

[11] L. Wu, S. Patankar, T. Morimoto, N. L. Nair, E. Thewalt, A. Little, J. G. Analytis, J. E. Moore, and J. Orenstein, Giant anisotropic nonlinear optical response in transition metal monopnictide Weyl semimetals, Nat. Phys. **13,** 350 (2017).

[12] E. J. Sie *et al.*, An ultrafast symmetry switch in a Weyl semimetal, Nature **565,** 61 (2019).

[13] M. Fox, *Optical Properties of Solids* (Oxford University Press, Oxford, 2010).

[14] F. Frostmann and R. R. Gerhardts, *Metal Optics near the Plasma Frequency* (Springer, Berlin, 2006).

[15] R. Tediosi, N. P. Armitage, E. Giannini, and D. van der Marel, Charge Carrier Interaction with a Purely Electronic Collective Mode: Plasmarons and the Infrared Response of Elemental Bismuth, Phys. Rev. Lett. **99,** 016406 (2007).

[16] N. P. Armitage, R. Tediosi, F. Levy, E. Giannini, L. Forro, and D. van der Marel, Infrared Conductivity of Elemental Bismuth under Pressure: Evidence for an Avoided Lifshitz-Type Semimetal-Semiconductor Transition, Phys. Rev. Lett. **104,** 237401 (2010).

[17] M. N. Ali, J. Xiong, S. Flynn, J. Tao, Q. D. Gibson, L. M. Schoop, T. Liang, N. Haldolaarachchige, M. Hirschberger, N. P. Ong, and R. J. Cava, Large, non-saturating magnetoresistance in WTe$_2$, Nature **514,** 205 (2014).

[18] Z. Zhu, X. Lin, J. Liu, B. Fauque, Q. Tao, C. Yang, Y. Shi, and K. Behnia, Quantum Oscillations, Thermoelectric Coefficients, and the Fermi Surface of Semimetallic WTe$_2$, Phys. Rev. Lett. **114,** 176601 (2015).

[19] C. C. Homes, M. N. Ali, and R. J. Cava, Optical properties of the perfectly compensated semimetal WTe$_2$, Phys. Rev. B **92,** 161109(R) (2015).

[20] A. J. Frenzel, C. C. Homes, Q. D. Gibson, Y. M. Shao, K. W. Post, A. Charnukha, R. J. Cava, and D. N. Basov, Anisotropic electrodynamics of type-II Weyl semimetal candidate WTe$_2$, Phys. Rev. B **95,** 245140 (2017).

[21] G. Autes, D. Gresch, M. Troyer, A. A. Soluyanov, and O. V. Yazyev, Robust Type-II Weyl Semimetal Phase in Transition Metal Diphosphides XP$_2$ (X = Mo, W), Phys. Rev. Lett. **117,** 066402 (2016).

[22] N. Kumar, Y. Sun, N. Xu, K. Manna, M. Yao, V. Suss, I. Leermakers, O. Young, T. Forster, M. Schmidt, H. Borrmann, B. Yan, U. Zeitler, M. Shi, C. Felser, and C. Shekhar, Extremely high magnetoresistance and conductivity in the type-II Weyl semimetals WP$_2$ and MoP$_2$, Nat. Commun. **8,** 1642 (2017).

[23] M. Y. Yao, N. Xu, Q. S. Wu, G. Autes, N. Kumar, V. N. Strocov, N. C. Plumb, M. Radovic, O. V. Yazyev, C. Felser, J. Mesot, and M. Shi, Observation of Weyl Nodes

in Robust Type-II Weyl Semimetal WP$_2$, Phys. Rev. Lett. **122**, 176402 (2019).

[24] H. Mathis, R. Glaum, and R. Gruehn, Reduction of WO$_3$ by phosphorus, Acta Chem. Scand. **45**, 781 (1991).

[25] See Supplemental Material at http://link.aps.org/supplemental/10.1103/PhysRevApplied.13.014058 for experimental and theoretical details as well as additional figures, tables, and discussions, which includes Refs. [32–35].

[26] A. B. Kuzmenko, Kramers–Kronig constrained variational analysis of optical spectra, Rev. Sci. Instrum. **76**, 083108 (2005).

[27] A. A. Soluyanov, D. Gresch, Z. Wang, Q. Wu, M. Troyer, X. Dai, and B. A. Bernevig, Type-II Weyl semimetals, Nature **527**, 495 (2015).

[28] K. Deng *et al.*, Experimental observation of topological Fermi arcs in type-II Weyl semimetal MoTe$_2$, Nat. Phys. **12**, 1105 (2016).

[29] S. Ahn, E. J. Mele, and H. Min, Electrodynamics on Fermi Cyclides in Nodal Line Semimetals, Phys. Rev. Lett. **119**, 147402 (2017).

[30] Y. Shao, Z. Sun, Y. Wang, C. Xu, R. Sankar, A. J. Breindel, C. Cao, M. M. Fogler, A. J. Millis, F. Chou, Z. Li, T. Timusk, M. B. Maple, and D. N. Basov, Optical signatures of Dirac nodal lines in NbAs$_2$, Proc. Natl. Acad. Sci. U.S.A. **116**, 1168 (2019).

[31] T. S. El-Bawab, *Optical Switching* (Springer, New York, 2006).

[32] D. J. Singh, *Planewaves, Pseudopotentials and the LAPW Method* (Kluwer Adademic, Boston, 1994).

[33] P. Blaha, K. Schwarz, G. Madsen, D. Kvasnicka, and J. Luitz, *An Augmented Plane Wave + Local Orbitals Program for Calculating Crystal Properties* (Technische Universitat Wien, Wien, 2001).

[34] L. M. Wei, K. H. Gao, X. Z. Liu, G. Yu, Q. W. Wang, T. Lin, S. L. Guo, Y. F. Wei, J. R. Yang, L. He, N. Dai, J. H. Chu, and D. G. Austing, Microwave-enhanced dephasing time in a HgCdTe film, Appl. Phys. Lett. **102**, 012108 (2013).

[35] J. Chu, S. Xu, and D. Tang, Energy gap versus alloy composition and temperature in Hg$_{1-x}$Cd$_x$Te, Appl. Phys. Lett. **43**, 1064 (1983).